FEAST: Fully Connected Expressive Attention for Spatial Transcriptomics

Supplementary Material

Contents

In the supplementary material, we begin with implementation details in Section A. Section A.1 describes the experimental setup, including hardware specifications and hyperparameters. Section A.2 details the data pre-processing steps, including the smoothing technique and target gene sets. Section B presents additional experimental analyses. Section B.1 provides the full ablation study results across all benchmark datasets. Section B.2 covers the analysis of various hyperparameters (e.g., k, τ_{neg}, β) and design choices, such as feature extractors. Finally, Section C presents additional qualitative visualizations, including detailed comparisons of PCC distributions and gene expression heatmaps.

A. Implementation Details

A.1. Experimental Setup

Framework and Hardware. Our framework was implemented using PyTorch and trained on a single NVIDIA RTX A6000 GPU. To ensure reproducibility and a fair comparison, we fixed the random seed to 3927, identical to the seed used in the official MERGE [4] implementation.

Off-grid Sampling Implementation. The original ST data provides integer grid coordinates (row, col) and their corresponding physical WSI coordinates. Our off-grid sampling strategy generates pseudo-spots at intermediate floating-point grid coordinates (e.g., extracting a spot at 17.5×25, between 17×25 and 18×25). Specifically, the generation process involves:

1. Computing the affine transformation matrix to map grid coordinates to physical WSI coordinates.
2. Generating candidate pseudo-spot coordinates at intermediate locations between the original grid coordinates.
3. Calculating the average nearest-neighbor distance among original spots.
4. Filtering candidates: To prevent sampling from background regions, we discard pseudo-spots whose distance to the nearest original spot exceeds the threshold derived in step 3.

Table 1. Hyperparameter configuration for FEAST training.

Config	Value
Architecture	
Input dimension (d)	1536
Number of attention heads (H)	8
Number of hierarchical layers (L)	3
Local neighborhood size (k)	32
Negative-aware Attention	
Negative scale factor (β)	1.5
Negative temperature (τ_{neg})	0.6
Positional bias slope (m_h)	$-2^{-1}, -2^{-2}, \ldots, -2^{-H}$
Optimization	
Optimizer	Adam
Learning rate	1×10^{-4}
Weight decay	1×10^{-5}
LR scheduler	Cosine Annealing
Epochs	1500

FEAST Training Workflow. To optimize training efficiency, we pre-extracted image embeddings using UNI2-h [2] for both original and pseudo-spots. Let N denote the total number of spots (original + pseudo) and d the feature dimension. For each WSI slide, we saved the features as a numpy array of shape (N, d). During the training of the FEAST framework, we directly load these pre-computed `.npy` files rather than processing raw images in real-time.

Hyperparameters. We provide a detailed summary of the hyperparameter configuration used for training FEAST in Table 1. All experimental results reported in the main text were obtained using this specific configuration.

A.2. Pre-processing

Smoothing. In this study, we applied the same SPCS [9] smoothing implementation and data preprocessing parameters as adopted in MERGE for fair comparison. Specifically, we set the zero cutoff parameter for gene filtering to 0.7. According to the analysis in MERGE, it was reported that only an average of about 5.72 genes per sample are excluded when this criterion (0.7) is applied. Consequently, to

Table 2. List of 250 target genes selected for each dataset.

Dataset	250 genes (Total genes to be predicted)
ST-Net	RPS3, IGLL5, RPLP1, TFF3, RPS18, GAPDH, TMSB10, RPLP2, RPS14, RPL37A, RPS19, RPL28, KRT19, RPL8, RPL13, RPL19, ACTB, RPL36, RPL18A, RPL35, RPL18, RPS2, RPS12, RPS21, RACK1, RPL13A, CTSD, FTL, PFN1, MGP, RPS15, RPS11, RPS16, HLA-B, UBA52, NHERF1, RPS17, PSAP, RPLP0, SERF2, RPS27, RPS8, RPL27A, MUC1, RPS28, H2AJ, RPL10, CALR, RPS29, RPL38, RPL11, P4HB, RPS6, CST3, FTH1, RPS4X, SSR4, RPL30, ERBB2, APOE, AZGP1, RPL3, COX6C, HLA-C, FAU, RPS9, EEF2, B2M, RPS5, RPL12, ACTG1, RPS27A, RPL37, RPL23, HLA-A, RPL31, RPL29, RPL7A, IFI27, PABPC1, CD74, BEST1, RPL32, FASN, S100A9, GPX4, RPL15, RPL27, MZT2B, RPL23A, HSPB1, MALAT1, RPS24, COL1A1, C4B, KRT18, CFL1, CD81, ALDOA, RPL35A, SYNGR2, PPP1CA, HLA-E, TAGLN, RPL9, CD63, RPS3A, LGALS3BP, IGFBP2, BST2, TPT1, EDF1, RPS25, ATP6V0B, TAPBP, GRINA, XBP1, S100A11, NBEAL1, AEBP1, CCND1, OAZ1, RPL14, TAGLN2, FN1, PPDPF, BCAP31, IFITM3, PRDX1, BGN, GNAS, PTMA, UBC, MZT2A, SLC25A6, RPS20, HSP90AB1, RPS10, MYL6, CLDN3, ATP6AP1, PRDX2, RPL24, GNB2, RPL34, RPL4, LMNA, NDUFA13, HLA-DRA, SNHG25, TIMP1, H1-0, RPS23, COX8A, KRT8, LY6E, ENO1, GRN, PTPRF, RPL7, UBB, BSG, ELOB, COX6B1, TMSB4X, C1QA, PRSS8, RPL5, UQCR11, RPS7, A2M, RPS15A, VIM, S100A6, NDUFA11, PSMD3, EVL, APOC1, H3-3B, ATP5F1E, PLXNB2, MYL9, TUBA1B, CTSB, ISG15, FLNA, RPS13, NDUFB9, EIF4A1, POLR2L, CYBA, CRIP2, EEF1D, ATP1A1, ELF3, TUFM, SH3BGRL3, STARD10, C3, GUK1, ZNF90, C12orf57, TLE5, SEC61A1, SDC1, PLD3, SPDEF, ARHGDIA, IFI6, LAPTM5, RPL41, CLU, GNAI2, PFDN5, RPL39, SSR2, COX4I1, RHOC, JUP, EIF4G1, FXYD3, TSPO, UQCRQ, COL1A2, RPL10A, S100A8, SELENOW, TPI1, ATP5MC2, PTMS, IGFBP5, LGALS1, SPINT2, RPSA, GSTP1, CHCHD2, EIF5A, COX5B, ATG10, RPL6, EEF1A1, CAPNS1, LMAN2, UBE2M, SPARC, EIF3C, GAS5, TUBB, ACTN4, IGFBP4
Her2ST	IGKC, TMSB10, ERBB2, IGHG3, IGLC2, IGHA1, GAPDH, ACTB, IGLC3, IGHM, SERF2, PSMB3, PFN1, ACTG1, KRT19, RACK1, MUCL1, CISD3, APOE, MIEN1, SSR4, CALR, PSAP, CTSD, FTL, FTH1, TPT1, PTPRF, UBA52, P4HB, BEST1, HLA-B, FAU, SLC9A3R1, FN1, COL1A1, EEF2, IGHG4, CALML5, CD74, B2M, FASN, S100A9, MGP, CFL1, PSMD3, IGHG1, HLA-A, S100A6, MYL6, COL1A2, PHB, TAGLN2, HLA-E, HLA-C, KRT7, CD63, SYNGR2, STARD3, PABPC1, GPX4, GRB7, SLC25A6, AEBP1, GNAS, NDUFB9, EDF1, CRIP2, DDX5, OAZ1, EIF4G1, LMNA, GNB2, CST3, PCGF2, SDC1, S100A11, PRDX1, GRINA, ATP6V0B, TFF3, HLADRA, EEF1D, AZGP1, PPP1CA, FLNA, COL3A1, ATP5E, SPDEF, AP000769.1, ALDOA, PLXNB2, TAGLN, TUBA1B, APOC1, PRRC2A, LAPTM5, PTMS, KRT18, IFI27, PLD3, ADAM15, C1QA, AES, TSPO, MLLT6, TAPBP, SCAND1, ATP1A1, CD81, SEC61A1, CLDN3, PPDPF, S100A14, BGN, C3, MZT2B, S100A8, MDK, PFDN5, H2AFJ, SH3BGRL3, ENO1, XBP1, CYBA, COX6B1, TRAF4, CD24, PRSS8, MMP14, MUC1, VIM, MIDN, SPINT2, BST2, TIMP1, GUK1, ACTN4, CTSB, COX4I1, CCT3, HNRNPA2B1, SEPW1, LY6E, SCD, HSPB1, EIF4G2, BSG, ZYX, TUBB, LASP1, CD99, COL6A2, H1FX, RALY, UBE2M, SPARC, ATG10, HSP90AB1, ORMDL3, LMAN2, CHCHD2, COX7C, ARHGDIA, VMP1, UBC, IGFBP2, COPE, NUPR1, PERP, KRT81, PPP1R1B, LGALS3BP, SSR2, KIAA0100, MYL9, CIB1, IDH2, STARD10, LGALS1, COX6C, GRN, MAP-KAPK2, GNAI2, KDELR1, COL18A1, UQCRQ, COX5B, ELOVL1, CHPF, CLDN4, C12orf57, LGALS3, HSP90AA1, JUP, A2M, NDUFB7, PGAP3, HSPA8, TCEB2, PEBP1, COPS9, ATP5G2, ATP6AP1, MYH9, LSM4, COX8A, UQCR11, ATP5B, DHCR24, PTBP1, EIF3B, NDUFA3, FKBP2, MMACHC, RABAC1, ISG15, PTMA, RRBP1, POSTN, C1QB, BCAP31, PSMB4, LAPTM4A, INTS1, FNBP1L, JTB, NBL1, HM13, SLC2A4RG, ROMO1, SERINC2, NDUFA11, RHOC, TXNIP, TYMP, NACA, HSP90B1, SNRPB, PFKL, VCP, ERGIC1, NUCKS1, PSMD8, CALM2, AP2S1, DBI, C4orf48, SDF4, TPI1
SCC	S100A8, KRT6A, KRT14, S100A9, KRT5, KRT6B, KRT16, KRT6C, KRT17, MT-CO3, S100A7, MT-CO2, SFN, S100A2, MT-CO1, ACTB, PERP, SPRR1B, KRT10, KRT1, EEF1A1, RPLP1, LGALS7B, LGALS7, COL1A1, FABP5, RPS12, HLA-B, MT-ND4, RPLP2, ACTG1, GJB2, B2M, TPT1, RPL13, MT-ATP6, RPS24, PFN1, KRTDAP, RPS6, DMKN, RPLP0, MT-ND3, RPL37A, DSP, CXCL14, RPS18, RPS17, RPS8, RPL13A, MT-CYB, RPL11, RPL27A, RPL28, MT-ND1, RPS27, RPL32, CSTA, RPL34, RPL31, COL1A2, RPL8, SBSN, TMSB10, ENO1, RPS14, RPL36, SPRR2A, RPL39, GSTP1, RPS27A, JUP, RPS19, RPL37, RPL27, RPL3, RPS29, COL3A1, RPS11, CSTB, RPL9, RACK1, ANXA2, RPL7A, RPL23, RPL19, S100A11, RPS2, RPS28, EEF2, ANXA1, CD74, PABPC1, LDHA, RPS3, RPL35A, DSC2, AQP3, RPS25, IFI27, CALML5, YWHAZ, RPL6, TMSB4X, RPS23, RPL12, S100A14, RPS4X, UBA52, SLPI, PKP1, RPL38, HLA-A, RPS13, LY6D, RPL24, ATP1B3, MYL6, GJB6, S100A6, HSPB1, RPL18, MT-ND2, SDC1, IVL, FTL, RPS3A, RPL10, RPS15A, PI3, RPL18A, S100A10, RPS7, S100A7A, RPL29, RPL26, RPL41, RPL4, RPL7, SPARC, VIM, PTMA, RPS20, MMP1, SH3BGRL3, RPL15, MYH9, GJA1, ITM2B, PPIA, RPL14, UBC, RPL5, CD44, AHNAK, RPL21, DSC3, CNFN, CD24, CFL1, COL17A1, HSP90AA1, RPS16, PKM, NACA, RPS5, ALDOA, H3F3B, S100A16, TAGLN2, HLA-C, TRIM29, LYPD3, FAU, LMNA, SPINK5, SPRR2E, RPL22, KRT2, CST3, DSG3, CLCA2, RPSA, DSG1, RPS9, NDRG1, AC090498.1, GRN, TXN, HSPA8, TGFBI, CTSB, SPRR2D, HLA-DRA, ACTN4, RPS21, EIF1, CTSD, ARPC2, CALML3, KLK7, CALM1, GNAS, DYNLL1, FLG, FLNA, DST, SLC2A1, PSAP, EIF4G2, EEF1B2, FGFBP1, LGALS1, ITGA6, MYL12B, TPI1, RPL10A, TMEM45A, BTF3, DSTN, RTN4, HNRNPA2B1, LAD1, ATP1A1, SERPINB3, PRDX1, COL6A1, ATP5E, PPDPF, TYMP, CD63, EIF5A, YWHAQ, PGK1, HLA-E, IFITM3, RPS26, IGFBP4, OAZ1, NPM1, LCE3D, FXYD3, MT2A, COL6A2, POLR2L, CD59, HNRNPK, RPL35, TMBIM6, HSP90AB1

Table 3. Ablation study on negative-aware attention and off-grid sampling strategy. The best results are in **bold**.

Negative	Off-grid	ST-Net			Her2ST			SCC		
		MSE ↓	MAE ↓	PCC ↑	MSE ↓	MAE ↓	PCC ↑	MSE ↓	MAE ↓	PCC ↑
		0.1156	0.2700	0.7200	0.6538	0.6505	0.4920	0.5010	0.5730	0.5908
✓		0.1144	0.2696	**0.7267**	0.6321	0.6401	0.4958	0.4955	0.5522	**0.5978**
	✓	0.1126	0.2607	0.7222	0.6308	0.6397	0.5020	0.5035	0.5575	0.5850
✓	✓	**0.1111**	**0.2603**	0.7224	**0.6158**	**0.6342**	**0.5194**	**0.4923**	**0.5462**	0.5971

Table 4. Performance variation according to the number of neighbors (k) in local attention. The best results are in **bold**.

k	ST-Net			Her2ST			SCC		
	MSE ↓	MAE ↓	PCC ↑	MSE ↓	MAE ↓	PCC ↑	MSE ↓	MAE ↓	PCC ↑
8	0.1138	0.2630	0.7176	0.6327	0.6440	0.4957	0.4920	**0.5438**	0.5975
16	0.1119	**0.2597**	**0.7237**	0.6211	0.6366	0.5118	**0.4887**	0.5475	**0.5987**
32	**0.1111**	0.2603	0.7224	**0.6158**	0.6342	**0.5194**	0.4923	0.5462	0.5971
64	0.1140	0.2645	0.7177	0.6203	0.6379	0.5122	0.4902	0.5538	0.5980
100	0.1122	0.2614	0.7207	0.6205	**0.6321**	0.5061	0.4904	0.5567	0.5979

Table 5. Impact of the temperature parameter (τ_{neg}) on model performance. The best results are in **bold**.

τ_{neg}	ST-Net			Her2ST			SCC		
	MSE ↓	MAE ↓	PCC ↑	MSE ↓	MAE ↓	PCC ↑	MSE ↓	MAE ↓	PCC ↑
0.6	**0.1111**	**0.2603**	**0.7224**	**0.6158**	**0.6342**	**0.5194**	**0.4923**	**0.5462**	**0.5971**
1.0	0.1128	0.2623	0.7191	0.6240	0.6374	0.5104	0.4926	0.5497	0.5944
1.4	0.1129	0.2624	0.7212	0.6236	0.6371	0.5064	0.4966	0.5481	0.5952

prevent the inadvertent removal of potentially informative genes and to maintain consistent experimental conditions with MERGE, we omitted the separate gene filtering step. All other SPCS parameters were also kept exactly identical to the MERGE settings.

Gene. All experimental evaluations were carried out based on the 250 target genes specified in TRIPLEX [3]. Detailed information regarding this specific gene set is provided in Table 2.

B. Extended Experimental Analysis

In this section, we provide additional experimental results and detailed analyses that complement the findings presented in the main paper. Specifically, to further demonstrate the robustness of our model's performance, we conducted experiments using different train/val/test splits of the same dataset used in the main paper.

B.1. Ablation Study

We present the complete ablation study results across all three benchmark datasets (ST-Net [5], Her2ST [1], and SCC [7]) to validate our proposed components. Table 3 summarizes the performance changes when the negative-aware attention and off-grid sampling strategy are selectively applied. The baseline model, which utilizes neither component, generally exhibits the lowest performance across all metrics. Introducing either component individually leads to performance gains compared to the baseline. Most importantly, our FEAST framework, which integrates both components, achieves the best or highly comparable results across all three datasets. For example, in the Her2ST dataset, the full model achieves the highest PCC of 0.5194, surpassing both the baseline (0.4920) and single-component variants. These results confirm that the off-grid sampling strategy and negative-aware attention are complementary and essential for robust gene expression prediction in diverse tissue environments.

B.2. Detailed Analysis of Design Elements

In addition to the ablation study, we conducted a series of experiments to analyze the impact of various hyperparameters and design choices.

Effect of Number of Neighbors (k). In the main paper, we reported the impact of the number of neighbors k in local k-NN Attention only for the Her2ST dataset. Here, we expand this analysis to all three datasets, with results summarized in Table 4. The results illustrate that performance generally improves as k increases, with the most robust results observed in the range of $k = 16$ to 32. Specifically, while $k = 16$ achieved the best performance in several metrics for ST-Net and SCC, $k = 32$ yielded the optimal results for Her2ST and remained highly competitive across the other datasets. Notably, further increasing the number of neighbors to $k = 64$ or 100 did not lead to consistent performance gains and, in several instances, resulted in marginal degradation. This suggests that an excessively large window may introduce noise from biologically distant spots. Considering the stable performance across all benchmarks and the computational efficiency, we selected $k = 32$ as the default value for FEAST.

Analysis of Temperature Scaling (τ_{neg}). We analyzed the variations in model performance with respect to the temperature parameter τ_{neg} in negative-aware attention. Table 5 presents the results for $\tau_{\text{neg}} \in \{0.6, 1.0, 1.4\}$. The experi-

Table 6. Impact of the negative attention scaling factor (β) on model performance. The best results are in **bold**.

β	ST-Net			Her2ST			SCC		
	MSE ↓	MAE ↓	PCC ↑	MSE ↓	MAE ↓	PCC ↑	MSE ↓	MAE ↓	PCC ↑
0.75	**0.1108**	**0.2565**	**0.7253**	0.6229	0.6358	0.5148	**0.4907**	0.5572	**0.6002**
1.5	0.1111	0.2603	0.7224	**0.6158**	**0.6342**	**0.5194**	0.4923	**0.5462**	0.5971
3.0	0.1155	0.2652	0.7088	0.6251	0.6397	0.5113	0.4969	0.5504	0.5952

Table 7. Performance comparison between different feature extractors. The best results are in **bold**.

Model	ST-Net			Her2ST			SCC		
	MSE ↓	MAE ↓	PCC ↑	MSE ↓	MAE ↓	PCC ↑	MSE ↓	MAE ↓	PCC ↑
UNI2-h [2]	**0.1111**	**0.2603**	**0.7224**	**0.6158**	**0.6342**	**0.5194**	0.4923	**0.5462**	0.5971
Prov-GigaPath [10]	0.1147	0.2645	0.7125	0.6279	0.6472	0.5121	**0.4914**	0.5468	**0.5988**

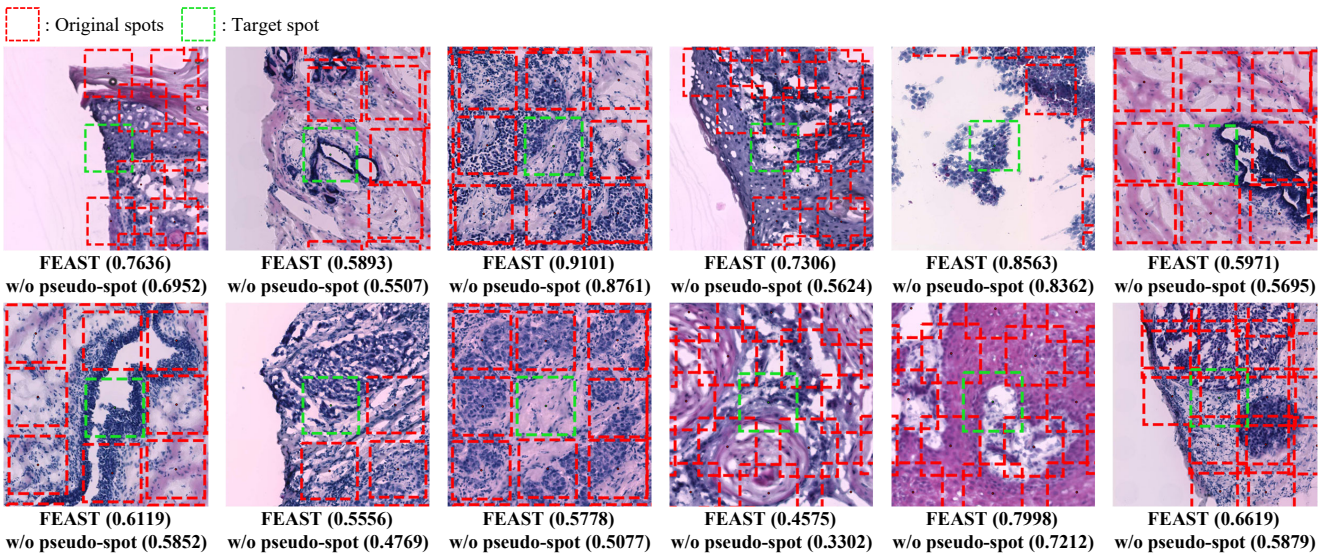

Figure 1. Additional illustration of the effect of pseudo-spots (off-grid sampling) on target spot prediction.

mental results show that $\tau_{neg} = 0.6$ consistently yields the best performance across all three datasets (ST-Net, Her2ST, and SCC) and all evaluation metrics. Specifically, increasing the temperature to 1.0 or 1.4 led to a general decline in both error metrics and correlation scores. This suggests that a lower temperature effectively sharpens the attention distribution and forces the model to focus only on the strongest negative relationships. Accordingly, we selected $\tau_{neg} = 0.6$ as the default value for FEAST, given its robust and superior performance across diverse tissue environments.

Impact of Negative Attention Scaling (β). We evaluated the impact of the hyperparameter β, which scales the contribution of the negative attention weights in our final attention computation. Table 6 presents the performance variations across different β values. The results indicate that the optimal β value varies across datasets; for instance, while $\beta = 0.75$ achieved the highest PCC scores for ST-Net (0.7253) and SCC (0.6002), $\beta = 1.5$ yielded the most robust performance for the Her2ST dataset. Notably, increasing β to 3.0 led to a consistent decline in performance across all benchmarks, suggesting that an excessive negative contribution may overshadow essential positive spatial relationships. Although we fixed $\beta = 1.5$ as the default for consistency in the main paper, these findings indicate that dataset-specific fine-tuning could yield further performance improvements.

Comparison of Feature Extractors. We compared UNI2-h [2] and Prov-GigaPath [10] as feature extractors for FEAST. As shown in Table 7, UNI2-h outperformed Prov-GigaPath in the majority of evaluation metrics, achieving the best results in 7 out of 9 cases across all datasets. While Prov-GigaPath showed marginal advantages in specific SCC metrics, UNI2-h demonstrated superior overall performance, particularly on the ST-Net and Her2ST. Consequently, we adopted UNI2-h as the default backbone for our framework due to its robust performance across most

benchmarks.

C. Additional Visualization

C.1. Efficacy of Off-grid Sampling

Figure 1 illustrates the comparative performance (PCC) of gene expression prediction with and without the application of pseudo-spots. The results demonstrate that incorporating pseudo-spots consistently leads to higher PCC values. Notably, this performance gain is most pronounced in challenging scenarios characterized by insufficient morphological context, such as regions with spatially sparse neighbors, tissue boundaries, or spots exhibiting structural patterns distinct from their surroundings.

C.2. Visualization of Negative-aware Attention

Figure 2 and Figure 3 visualize the attention maps for the target spot with and without the use of negative-aware attention. With the introduction of this mechanism, the model assigns positive weights to biologically similar regions while simultaneously assigning negative weights to tissues with distinct gene expression patterns. This demonstrates that the model does not indiscriminately assign positive weights based on spatial proximity, but rather accurately discriminates between positive and negative relationships.

C.3. PCC Comparison

We conducted a comparative analysis on the Her2ST dataset to evaluate the PCC performance for two key cancer-associated genes, FASN and GNAS [6, 8]. As illustrated in Figure 4, FEAST demonstrated a robust correlation capability, consistently outperforming MERGE across the majority of slide samples. While the legend indicates the superior average PCC of our method, a more granular look reveals that FEAST maintains high correlation scores even in instances where MERGE yields negative values. Quantitatively, FEAST surpassed the baseline in 33 and 28 out of the 36 total samples for FASN and GNAS, respectively.

This performance gap is visually summarized in Figure 5. The PCC distribution for FEAST is concentrated in the positive high-value region, standing in contrast to MERGE. This rightward shift in the distribution highlights FEAST's ability to consistently generate accurate gene expression predictions while minimizing instances of negative PCC values.

C.4. Gene Expression Comparison

Figure 6 and Figure 7 present the predicted gene expression heatmaps for FASN and GNAS, respectively, comparing FEAST and MERGE against the ground truth. Visual inspection reveals that FEAST generates predictions that are significantly closer to the ground truth than those of MERGE. Notably, FEAST accurately captures individual spots with expression characteristics distinct from their surroundings, demonstrating the superior spatial resolution of our model.

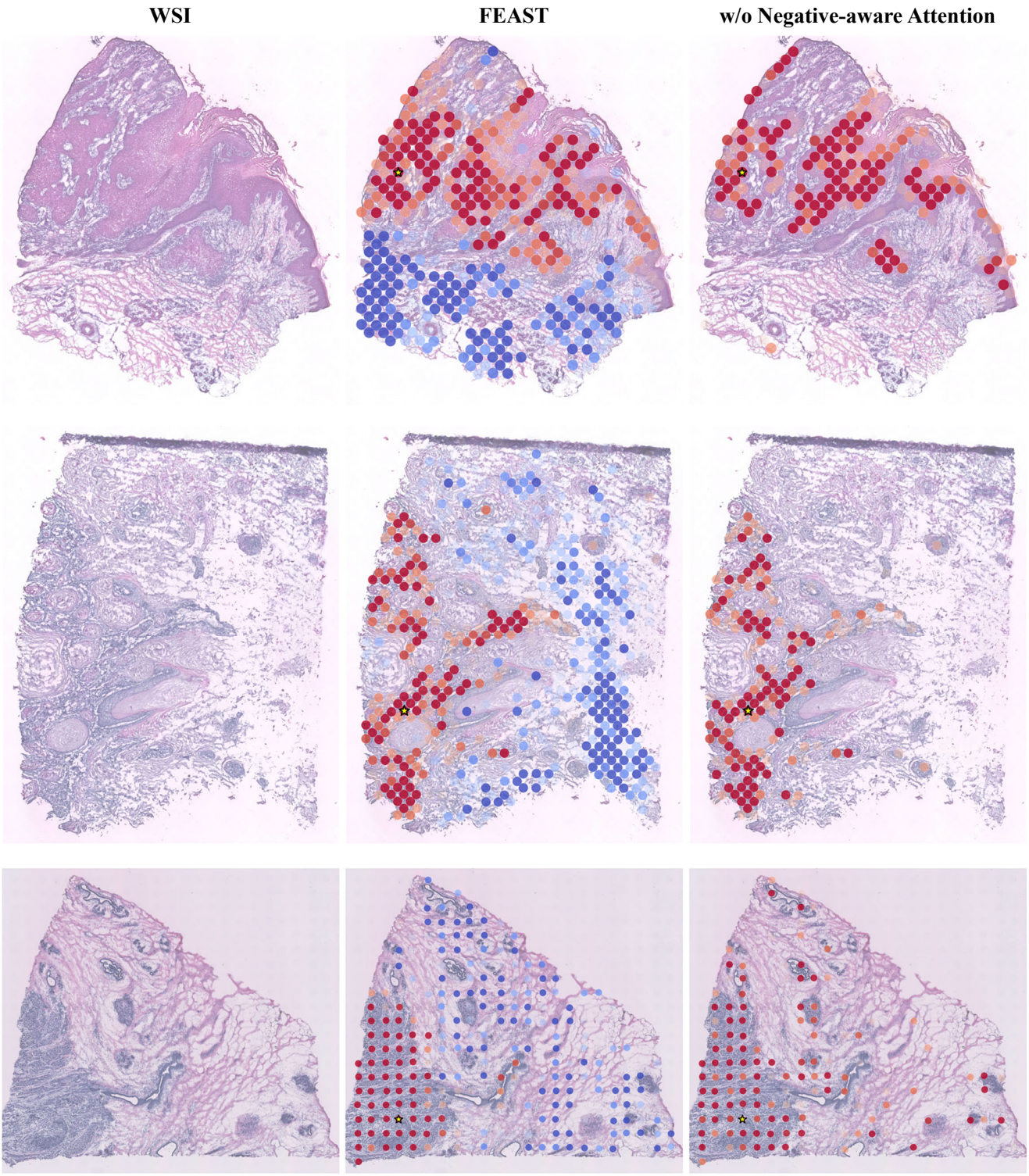

Figure 2. Comparison of attention maps with and without negative-aware attention.

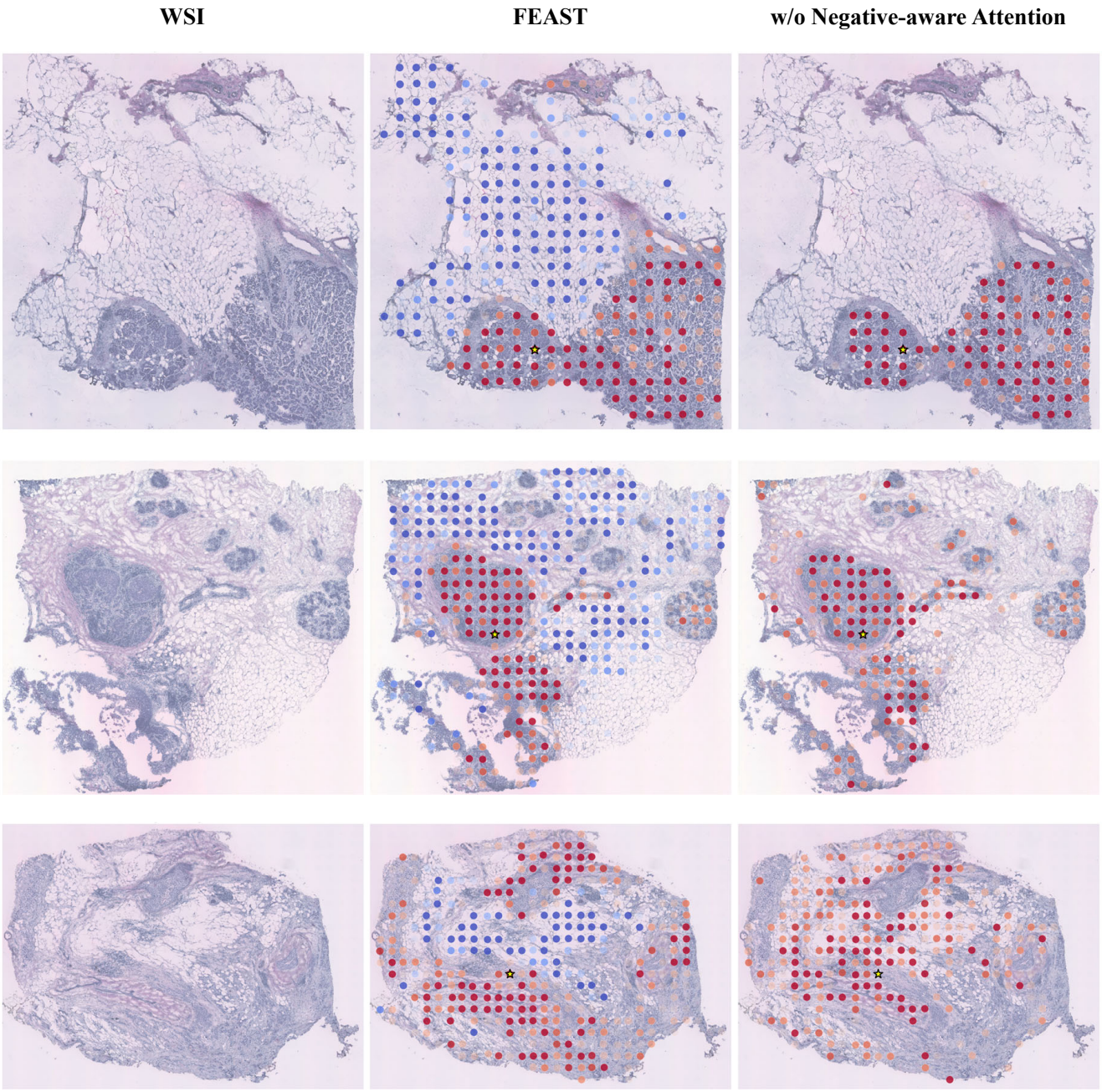

Figure 3. Comparison of attention maps with and without negative-aware attention.

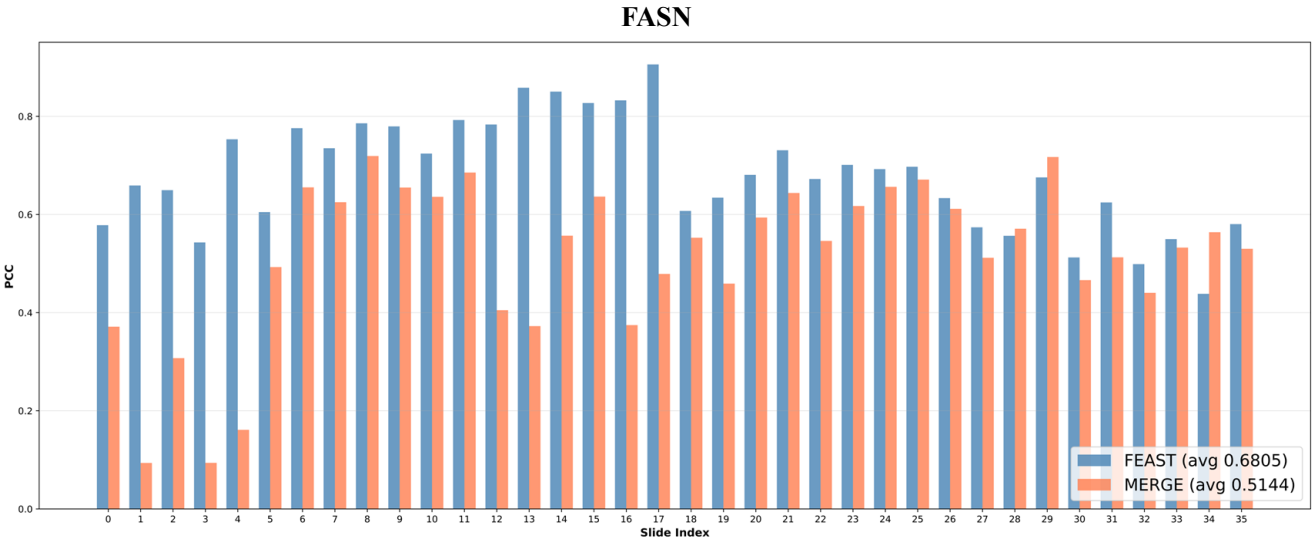

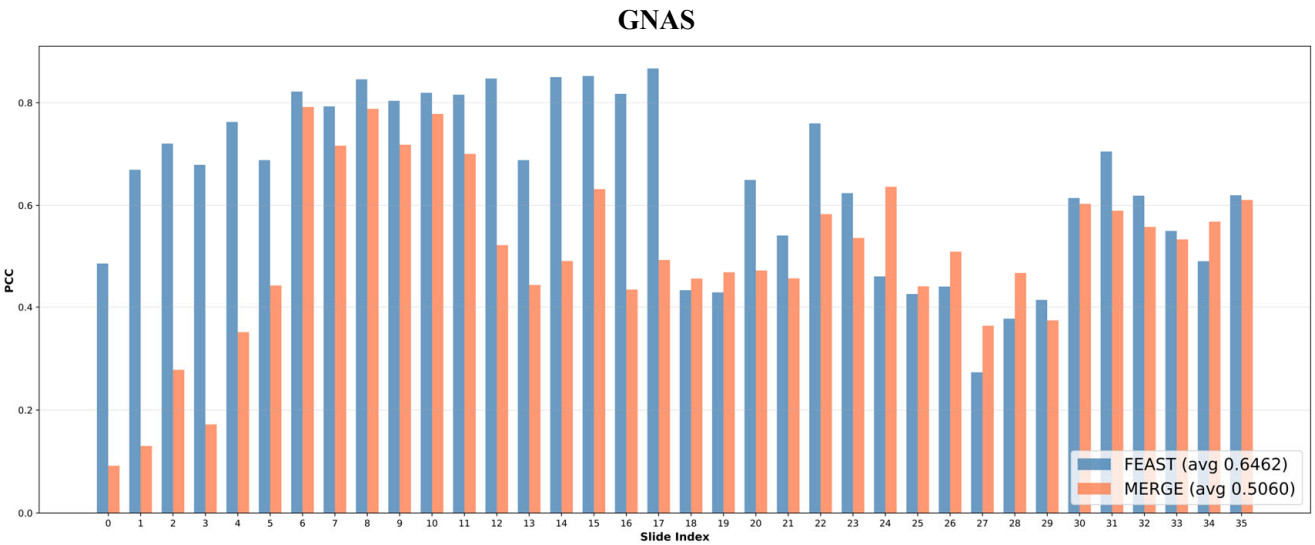

Figure 4. Bar plots of PCC scores for predicted FASN and GNAS gene expressions for each sample in the ST-Net dataset. The average PCC across the entire dataset is indicated in parentheses within the legend.

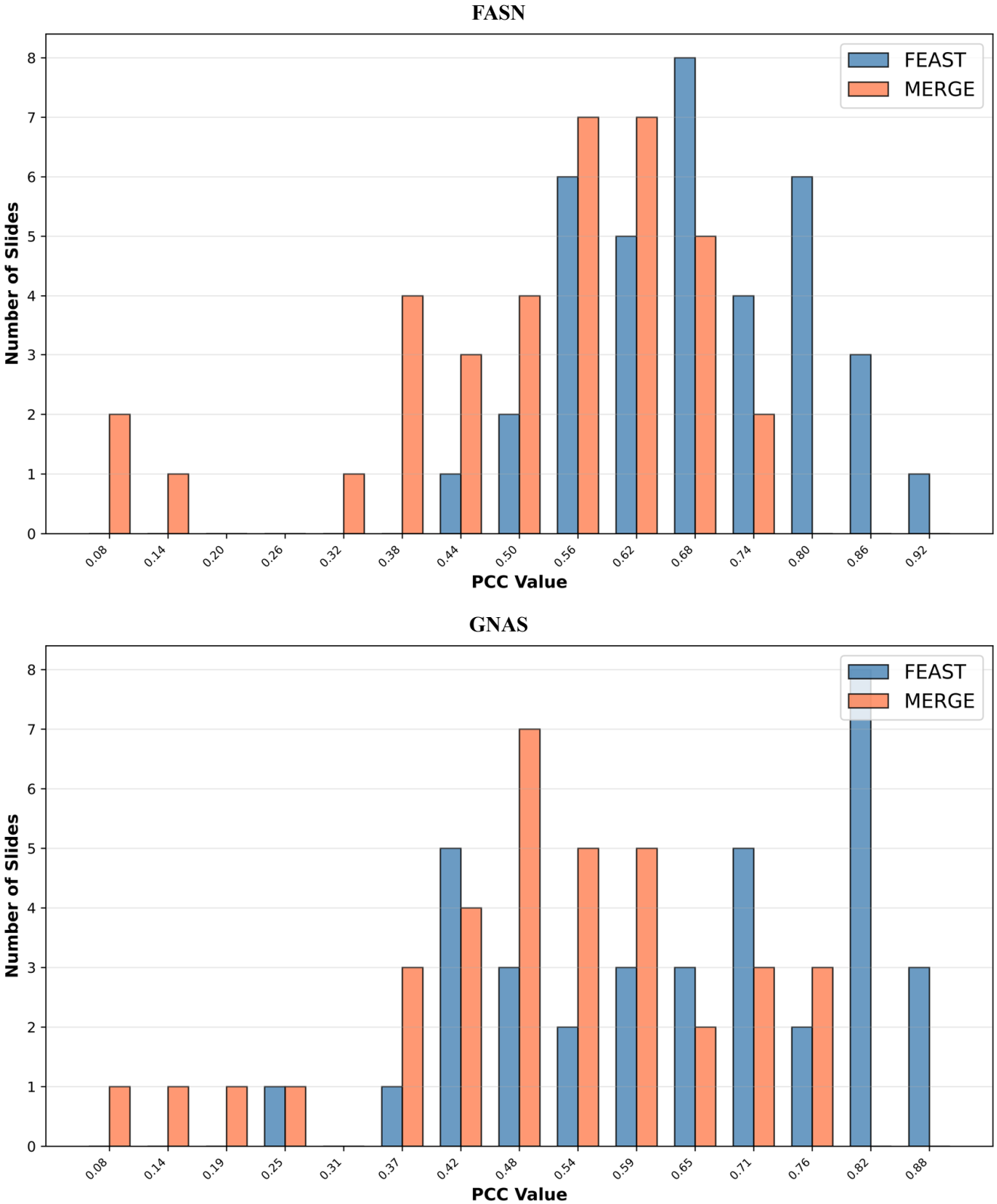

Figure 5. Histograms of PCC scores for FASN and GNAS predictions by the two methods on the ST-Net dataset. The distributions show that FEAST achieves higher PCC values compared to MERGE. Notably, it is evident that FEAST rarely yields negative PCC values.

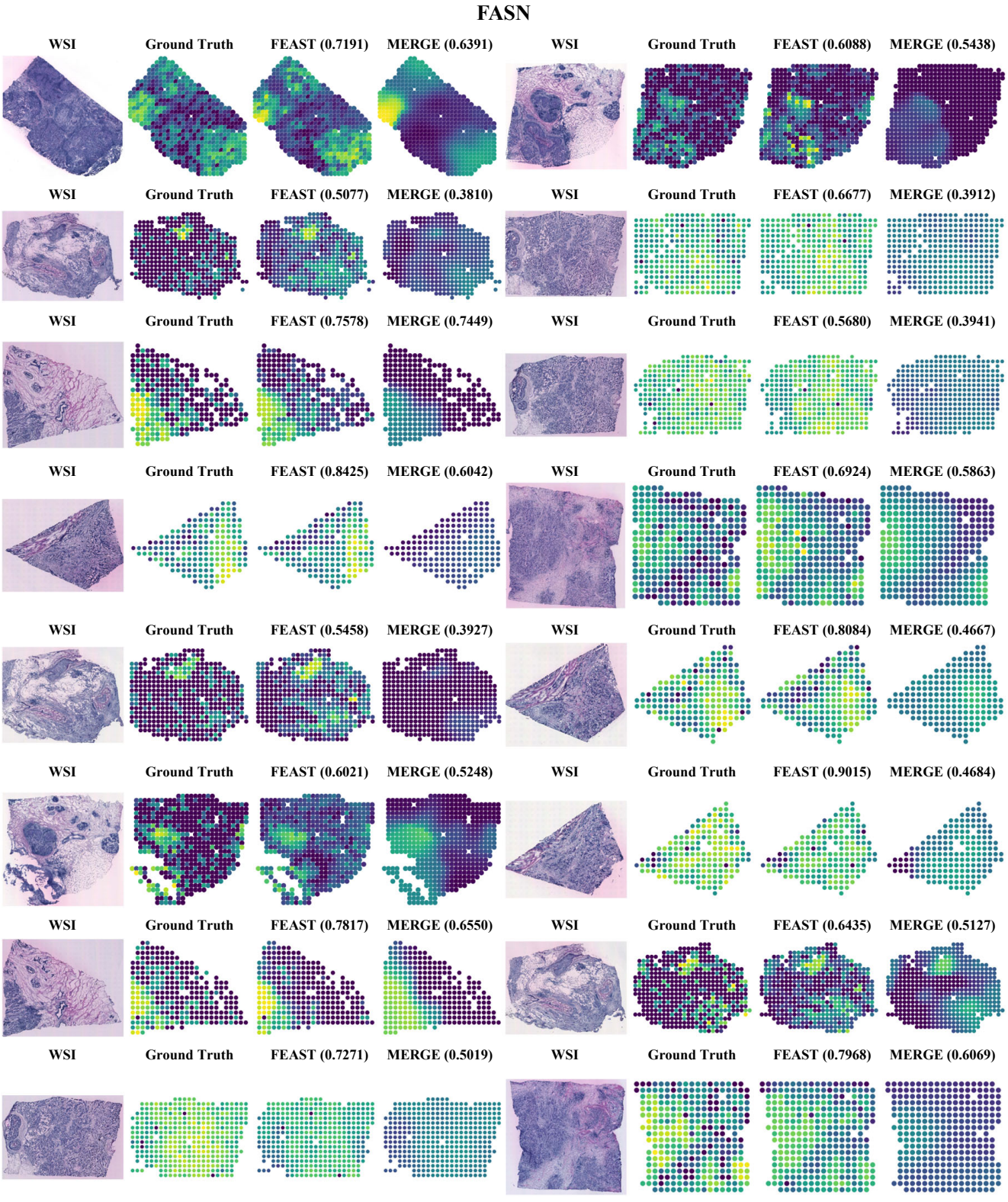

Figure 6. Qualitative comparison of predicted FASN gene expression heatmaps.

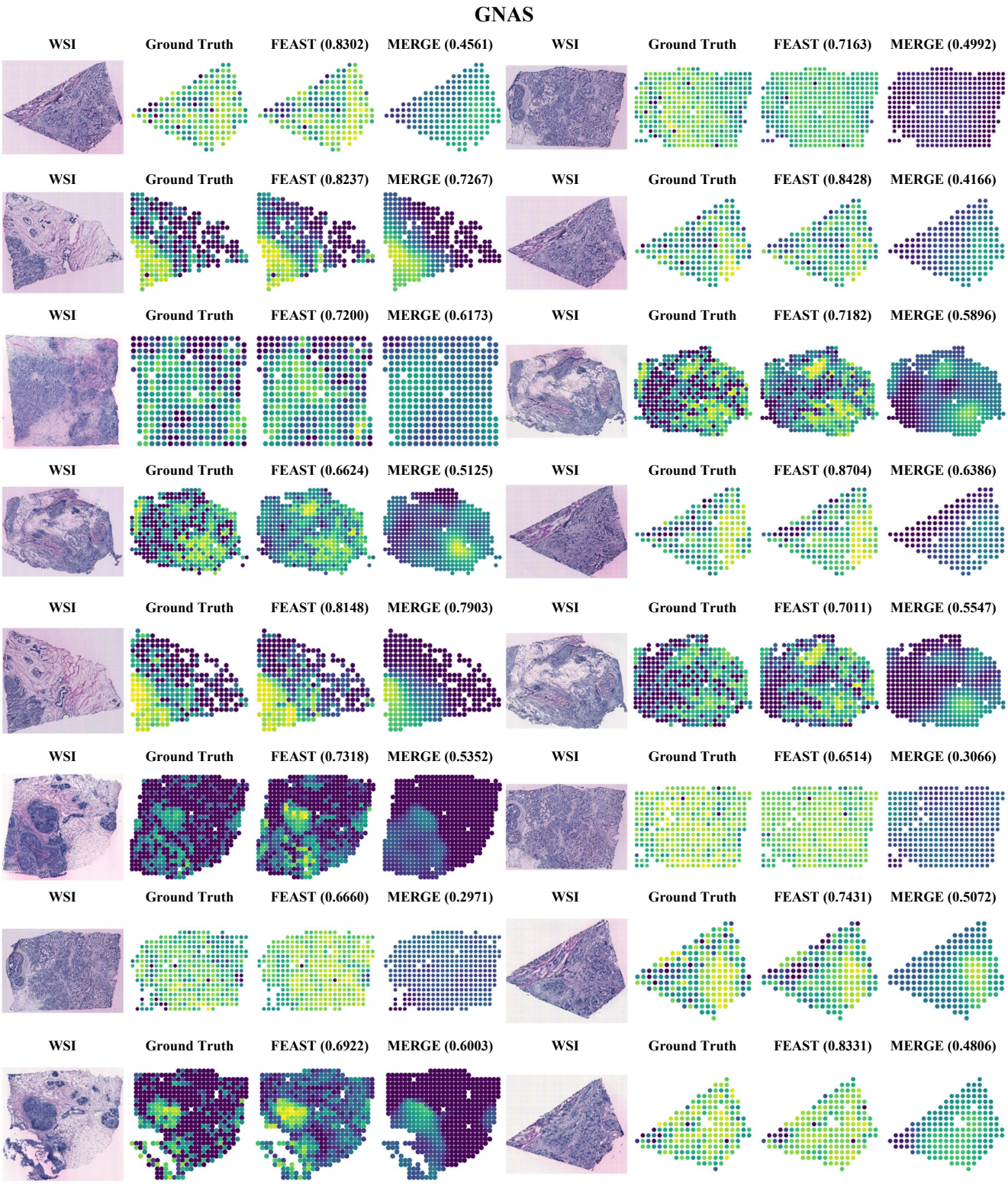

Figure 7. Qualitative comparison of predicted GNAS gene expression heatmaps.

References

[1] Alma Andersson, Ludvig Larsson, Linnea Stenbeck, Fredrik Salmén, Anna Ehinger, Sunny Wu, Ghamdan Al-Eryani, Daniel Roden, Alex Swarbrick, Åke Borg, et al. Spatial deconvolution of her2-positive breast tumors reveals novel intercellular relationships. *bioRxiv*, pages 2020–07, 2020. 3

[2] Richard J Chen, Tong Ding, Ming Y Lu, Drew FK Williamson, Guillaume Jaume, Andrew H Song, Bowen Chen, Andrew Zhang, Daniel Shao, Muhammad Shaban, et al. Towards a general-purpose foundation model for computational pathology. *Nature medicine*, 30(3):850–862, 2024. 1, 4

[3] Youngmin Chung, Ji Hun Ha, Kyeong Chan Im, and Joo Sang Lee. Accurate spatial gene expression prediction by integrating multi-resolution features. In *Proceedings of the IEEE/CVF Conference on Computer Vision and Pattern Recognition*, pages 11591–11600, 2024. 3

[4] Aniruddha Ganguly, Debolina Chatterjee, Wentao Huang, Jie Zhang, Alisa Yurovsky, Travis Steele Johnson, and Chao Chen. Merge: Multi-faceted hierarchical graph-based gnn for gene expression prediction from whole slide histopathology images. In *Proceedings of the Computer Vision and Pattern Recognition Conference*, pages 15611–15620, 2025. 1

[5] Bryan He, Ludvig Bergenstråhle, Linnea Stenbeck, Abubakar Abid, Alma Andersson, Åke Borg, Jonas Maaskola, Joakim Lundeberg, and James Zou. Integrating spatial gene expression and breast tumour morphology via deep learning. *Nature biomedical engineering*, 4(8): 827–834, 2020. 3

[6] Dirk A Hunt, Hilary M Lane, Matthew E Zygmont, Peter A Dervan, and Randolph A Hennigar. Mrna stability and overexpression of fatty acid synthase in human breast cancer cell lines. *Anticancer research*, 27(1A):27–34, 2007. 5

[7] Andrew L Ji, Adam J Rubin, Kim Thrane, Sizun Jiang, David L Reynolds, Robin M Meyers, Margaret G Guo, Benson M George, Annelie Mollbrink, Joseph Bergenstråhle, et al. Multimodal analysis of composition and spatial architecture in human squamous cell carcinoma. *cell*, 182(2): 497–514, 2020. 3

[8] X Jin, L Zhu, Z Cui, J Tang, M Xie, and G Ren. Elevated expression of gnas promotes breast cancer cell proliferation and migration via the pi3k/akt/snail1/e-cadherin axis. *Clinical and Translational Oncology*, 21(9):1207–1219, 2019. 5

[9] Yusong Liu, Tongxin Wang, Ben Duggan, Michael Sharpnack, Kun Huang, Jie Zhang, Xiufen Ye, and Travis S Johnson. Spcs: a spatial and pattern combined smoothing method for spatial transcriptomic expression. *Briefings in Bioinformatics*, 23(3), 2022. 1

[10] Hanwen Xu, Naoto Usuyama, Jaspreet Bagga, Sheng Zhang, Rajesh Rao, Tristan Naumann, Cliff Wong, Zelalem Gero, Javier González, Yu Gu, et al. A whole-slide foundation model for digital pathology from real-world data. *Nature*, 630(8015):181–188, 2024. 4